Journal of Materials Chemistry A

ROYAL SOCIETY OF CHEMISTRY

PAPER

View Article Online
View Journal | View Issue



Cite this: J. Mater. Chem. A, 2025, 13, 7313

# Electroless-deposited NiFeP catalyst-coated-membrane cathodes for anion exchange membrane water electrolysis†

Kaiming Guo, [a] Masahiro Kunimoto[b] and Takayuki Homma *[ac]

The rational design of membrane electrode assemblies is crucial for anion exchange membrane (AEM) water electrolysis. In this study, a series of NiFeP catalyst-coated-membranes (CCMs) were synthesized using a Pd-catalyzed electroless deposition method, which served as a cathode for an AEM water electrolyzer. This electroless deposition method enables the *in situ* growth of NiFeP electrocatalysts on the AEM surface, thus mitigating the degradation of the ionomer/binder during long-term water electrolysis and decreasing the resistance of the membrane electrode assembly. The $Ni_{0.79}Fe_{0.08}P_{0.13}$ electrocatalyst delivered −500 mA $cm^{-2}$ at an overpotential of −0.47 V in 1.0 M $K_2CO_3$, exhibiting outstanding hydrogen evolution reaction (HER) performance. Furthermore, the $Ni_{0.79}Fe_{0.08}P_{0.13}$ electrocatalyst demonstrated excellent stability by maintaining −500 mA $cm^{-2}$ for over 100 h with only a 5.7% increase in overpotential. The exceptional HER catalytic performance of the $Ni_{0.79}Fe_{0.08}P_{0.13}$ electrocatalyst was attributed to the optimized electronic structure resulting from Fe incorporation and the formation of amorphous regions, which enhanced the catalytic performance and facilitated hydrogen diffusion. This work offers new insights into the fabrication and analysis of ionomer/binder-free CCMs for improving the performance of AEM water electrolysis devices.

Received 26th September 2024
Accepted 25th January 2025

DOI: 10.1039/d4ta06868h

rsc.li/materials-a



## Introduction

The contradiction between increasing energy demands and depletion of fossil fuels creates great challenges for modern society, thus emphasizing the importance of developing reliable sustainable energy resources.[1] Hydrogen ($H_2$), which is advantageous due to its high energy content and environment friendliness, emerges as a versatile energy carrier.[2,3] It facilitates the storage of renewable resources like solar and wind in the form of hydrogen, which can conveniently release energy in fuel cell systems to meet diverse energy consumption requirements. All these advantages contribute to the attractiveness of industrial hydrogen production technologies, for example, like low-temperature water electrolysis.

Low-temperature water electrolysis encompasses three major technologies: proton exchange membrane (PEM) water electrolysis, alkaline water electrolysis and anion exchange membrane (AEM) water electrolysis.[4] The key advantage of PEM water electrolysis is the usage of PEM, which not only sufficiently separates the cathode side and anode side to avoid the mixing of $H_2$ and $O_2$, but offers a fast proton transportation. Alkaline water electrolysis offers the advantage of employing an alkaline solution, which allows the usage of non-noble metal materials, resulting in lower costs. Anion exchange membrane (AEM) water electrolysis is gaining increasing interest for combining the advantages of proton exchange membrane (PEM) water electrolysis and alkaline water electrolysis.[4,5] As a result, AEM water electrolyzers are expected to efficiently generate high-purity $H_2$ at a relatively low cost by employing an alkaline electrolyte. However, research on AEM water electrolysis is still in the early stages, with several challenges remaining to achieve highly active and stable electrolyzers.

The design of membrane electrode assemblies (MEAs), incorporating optimized catalysts and configurations, plays an essential role in the performance of AEM water electrolyzers.[6–8] It is vital to select an electrocatalyst for MEAs which is expected to give a high current density (over 0.5 A $cm^{-2}$) at low potential, for industrial applications.[9,10] NiFeP has been widely reported as an efficient catalyst for the hydrogen evolution reaction (HER). For example, Wei *et al.* synthesized a NiFeP catalyst on Cu foam *via* optimized electrodeposition using a deep eutectic solvent. This process involves the dissolution of a Fe anode (FA) to supply Fe. Ni nitrite (NN) is also added as a Ni source for electrodeposition. The resulting NiFeP_FA_NN electrocatalyst demonstrated excellent HER activity by delivering −10 mA $cm^{-2}$

[a]Department of Applied Chemistry, Waseda University, Shinjuku, Tokyo 169-8555, Japan. E-mail: t.homma@waseda.jp
[b]Global Center for Science and Engineering, Waseda University, Shinjuku, Tokyo 169-8555, Japan
[c]Research Organization for Nano & Life Innovation, Waseda University, Shinjuku, Tokyo 162-0041, Japan

† Electronic supplementary information (ESI) available. See DOI: https://doi.org/10.1039/d4ta06868h

at an overpotential of 56 mV.[11] Zhang *et al.* synthesized the $(Fe_{0.048}Ni_{0.952})_2P$ catalyst *via* phosphorization of FeNi-LDH, which demonstrated enhanced HER activity in acidic, neutral, alkaline media by achieving $-10$ mA cm$^{-2}$ at overpotentials of 81, 90, and 103 mV, respectively.[12] These studies highlight the potential of the NiFeP catalyst as an excellent HER catalyst. However, the underlying mechanism behind its high activity toward the HER remains unclear and requires further investigation.

Regarding the configuration of MEAs, a recent study indicates that using a catalyst-coated substrate (CCS) anode paired with a catalyst-coated membrane (CCM) cathode yields optimal performance in the AEM water electrolyzer, particularly with regard to cell voltage.[13] However, synthesizing a metal phosphorous film on the AEM for the fabrication of CCM cathodes is challenging because of the unfavorable physical properties of AEMs during fabrication processes, such as their nonconductive nature and limited thermal stability.[14] Traditionally, ionomers/binders are crucial to combine the catalyst with the AEM. However, they can restrict the exposure of active sites and degrade during prolonged water electrolysis.[15–17] Identifying strategies to avoid the disadvantages of using ionomers/binders is necessary for advancing AEM water electrolyzer technology. In this context, electroless deposition is a powerful technique that enables the *in situ* growth of metallic materials on the surface of a nonconductive substrate without the need for an ionomer/binder. In 2021, our group reported a novel process to form Pd nuclei on the AEM surface, catalyzing electroless Ni deposition.[18] More recently, Kong *et al.* reported an efficient electroless-deposited NiFe CCM for the oxygen evolution reaction with reduced cell resistance and enhanced durability, attributed to its ionomer-free structure, further validating the superiority of electroless-deposited CCMs.[19] However, research on fabricating CCMs *via* electroless deposition for AEM water electrolysis remains limited, and the properties of CCMs fabricated *via* Pd-catalyzed electroless deposition are not fully explored.

Considering the membrane stability and corrosion risks of AEM water electrolyzers, the pH value of the electrolyte should be maintained as low as possible. Faraj *et al.* and Pavel *et al.* reported stable water electrolysis with a combination of $K_2CO_3$ solution (pH = 10–12) and AEM.[20,21] Ito *et al.* suggested that the performance of the electrolyzer with $K_2CO_3$ solution (pH value around 12) was more stable and superior than that with KOH at a low pH value of 12.[22] Meanwhile, they demonstrated that the utilization of less-corrosive $K_2CO_3$ solution enables the utilization of general purpose materials like stainless steel for pipes or tanks, thus decreasing the possibility of electrolyte leakage. Based on the insights from studies above, 1.0 M $K_2CO_3$ solution (pH value around 12) appears to be a promising electrolyte for AEM water electrolyzers.

Herein, a series of NiFeP electrocatalysts were synthesized on AEMs *via* a facile Pd-catalyzed electroless deposition to unveil the origin of their superior HER performance in an AEM water electrolyzer fed with 1.0 M $K_2CO_3$ solution. Electrochemical measurements were performed to evaluate the catalytic performance and stability of the as-prepared catalysts. The underlying reasons for the high activity and excellent stability of the as-prepared NiFeP electrocatalysts were explored *via* characterization studies. Benefiting from the Fe introduction, the NiFeP electrocatalyst's electronic structure was significantly tailored, potentially altering the role of the Ni sites during the HER. Moreover, the Fe content significantly influenced the crystallinity of the NiFeP electrocatalysts, increasing the number of amorphous/crystalline interfaces. This increased the number of active sites and optimized HER performance.

## Experimental section

### Materials and reagents

Ammonium sulfate ($(NH_4)_2SO_4$, ≥99.5%), citric acid monohydrate ($C_6H_6Na_3O_7$, ≥99.5%), iron(II) sulfate heptahydrate ($FeSO_4\cdot7H_2O$, ≥99.0%), nickel(II) sulfate hexahydrate ($NiSO_4\cdot6H_2O$, ≥99.0%), sodium phosphate monohydrate ($NaH_2PO_2\cdot H_2O$, ≥82.0% as $NaH_2PO_2$), palladium(II) chloride ($PdCl_2$, ≥99.0%), hydrochloric acid (HCl, 36%), and sodium hydroxide (NaOH, ≥97.0%) were purchased from Kanto Chemical Co., Inc. (Japan). Dimethylamine borane ($(CH_3)_2NH\cdot BH_3$, DMAB, ≥97.0%) was purchased from Fujifilm Wako Pure Chemical Corp. (Japan). All reagents were used without further purification. Ultrapure water (18.2 MΩ cm @ 25 °C) was generated using a Milli-Q IQ 7003 (MERCK Co. Ltd.) system.

### Preparation of the CCM cathode

NiFeP electrocatalysts (10 mm × 10 mm) were synthesized on the AEM surface *via* electroless deposition, as shown in Scheme 1. The detailed procedure is as follows. First, a 30 mm × 30 mm AEM (A-201, Tokuyama Corp.) was masked with polytetrafluoroethylene (PTFE) tape, leaving only one side of the central region (10 mm × 10 mm) exposed. Subsequently, the masked AEM was rinsed with ultrapure water for 15 s, followed by immersion in a 0.2 g L$^{-1}$ $PdCl_2$ solution (dissolved in 2.5 mL L$^{-1}$ of 36% HCl) and 0.02 M DMAB for 30 s and 10 s, respectively. During this step, a change in color from yellow to dark brown was observed in the exposed area (Fig. S1a and b†), indicating the adsorption of Pd species and the formation of Pd nuclei on the AEM surface. Next, $FeSO_4\cdot7H_2O$ (2.5 mmol, 5 mmol, 7.5 mmol),

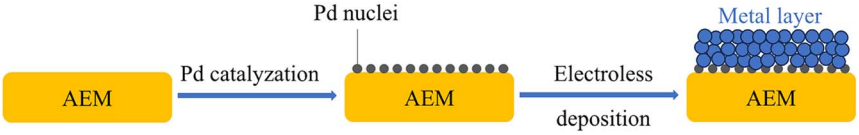


Scheme 1 Synthesis of metal films on anion exchange membranes (AEMs) by electroless deposition.

 

$NiSO_4 \cdot 6H_2O$ (7.5 mmol, 5 mmol, 2.5 mmol), $NaH_2PO_2 \cdot H_2O$ (20 mmol), $(NH_4)_2SO_4$ (40 mmol), and $C_6H_5Na_3O_7$ (10 mmol) were completely dissolved in 50 mL of ultrapure water with continuous stirring. The pH was adjusted to 10 using NaOH, and the solution volume was brought up to 100 mL with ultrapure water. Notably, the total molar amount of $FeSO_4 \cdot 7H_2O$ and $NiSO_4 \cdot 6H_2O$ was kept constant at 10 mmol. Finally, the pretreated AEM was immersed in the bath at 70 °C for 15 min, forming NiFeP electrocatalysts on the exposed area (Fig. S1c†). For comparison, another electrocatalyst was fabricated using the same process with 5 mmol $NiSO_4 \cdot 6H_2O$ but without using $FeSO_4 \cdot 7H_2O$ in the electroless deposition bath. The Pt/C noble electrocatalyst (3.0 mg $cm^{-2}$, Fig. S1d†) on the AEM used in this study was fabricated *via* the spraying method, as described in previous studies.[13,23]

### Characterization and electrochemical tests

The surface morphology and composition of the as-prepared electrocatalysts were analyzed using scanning electron microscopy (SEM, SU 8240, Hitachi) equipped with energy-dispersive X-ray spectroscopy (EDS). Cross-sectional SEM was employed to measure the thickness of the deposits. A focused ion beam (FIB, JIB-4000, JEOL, Ltd.) was used to cut the metal films into small flakes. Transmission electron microscopy (TEM, JEM2100F, JEOL Ltd.) images with selected area electron diffraction (SAED) patterns were obtained to investigate lattice fringes and defects in the as-prepared electrocatalysts, while mapping images provided insights into the elemental distribution across the metal film. X-ray diffraction (XRD, SmartLab 9 kW, Rigaku) analysis was conducted to determine the phases present in the electrocatalyst samples. To evaluate the species and composition of both the bulk material and the interface between the metal film and AEM, depth profiling of X-ray photoelectron spectroscopy (XPS) was performed using an X-ray photoelectron spectrometer (Micro-XPS, VersaProbe II, ULVAC-PHI).

Electrochemical measurements were conducted using an HZ-pro electrochemical workstation (Meiden Hokuto Co., Ltd.) in a 1.0 M $K_2CO_3$ solution. The previously reported YNU cell configuration is shown in Scheme 2 (picture shown in Fig. S2†).[24] In the YNU cell setup, the as-prepared electrocatalyst, a saturated Ag/AgCl electrode, and Ni foam (NF) served as the working, reference, and counter electrodes, and the MEA structure is denoted as electrocatalyst|AEM|NF. Carbon paper was used as the gas diffusion layer (GDL) on the cathode side, and the as-prepared NiFeP electrocatalyst served as the cathode. Ni foam acted as both the anode and the GDL. The electrolyte was circulated only on the anode side to ensure relatively dry hydrogen production on the cathode side. Linear sweep voltammetry (LSV) was conducted at a scan rate of 10 mV $s^{-1}$. The Tafel plots were generated by applying the following equation to convert the polarization curves:

$$\eta = b \log|i| + a. \quad (1)$$

in this equation, $\eta$, $i$, and $b$ represent the overpotential, current density, and Tafel slope, respectively. The electrochemical double-layer capacitance ($C_{dl}$) of the prepared catalyst was calculated from cyclic voltammetry (CV) data obtained at various scan rates (20–100 mV $s^{-1}$). The ohmic resistances ($R_{ohm}$) of the electrocatalysts were measured by electrochemical impedance spectroscopy (EIS) using a membrane test system (MTS740, Toyo Corp., Japan). This membrane test system enables through-plane impedance measurement of a single membrane, effectively avoiding influences from other components typically present in a MEA. The catalyst stability was evaluated using chronopotentiometry (CP) throughout 100 h. The potential values were converted to the reversible hydrogen electrode (RHE) reference using the following equation:

$$E\,(vs.\ \mathrm{RHE}) = E\,(vs.\ \mathrm{Ag/AgCl}) + 0.197 + 0.059\ \mathrm{pH}. \quad (2)$$

The faradaic efficiency (FE) was calculated using the following equation:

$$\eta_{FE} = (m \times z \times F)/Q. \quad (3)$$

where $m$, $z$, $F$ and $Q$ represent the moles of $H_2$ product, transferred electrons, faradaic constant and consumed charge, respectively. The $H_2$ gas was collected from the YNU cell at a current of 0.5 A by the water drainage method, and the anode and cathode of the electrolyzer were fed with 1.0 M $K_2CO_3$ solution and ultrapure water, respectively.

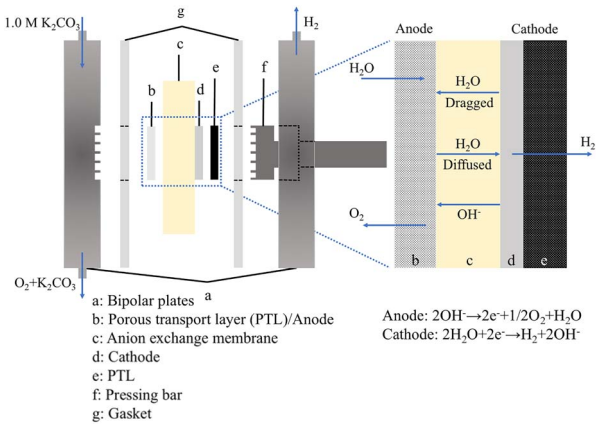


Scheme 2 Structure of the test cell and membrane electrode assemblies (MEAs) for anion exchange membrane (AEM) water electrolysis.

## Results and discussion

The precise composition of the as-prepared NiFeP electrocatalyst was determined using EDS (Table S1†). The electrocatalysts $Ni_{0.74}Fe_{0.12}P_{0.14}$, $Ni_{0.79}Fe_{0.08}P_{0.13}$, $Ni_{0.84}Fe_{0.07}P_{0.09}$, and $Ni_{0.85}P_{0.15}$ correspond to electroless deposition baths containing 2.5 mmol of $NiSO_4 \cdot 6H_2O$ and 7.5 mmol of $FeSO_4 \cdot 7H_2O$, 5 mmol of $NiSO_4 \cdot 6H_2O$ and 5 mmol of $FeSO_4 \cdot 7H_2O$, 7.5 mmol of $NiSO_4 \cdot 6H_2O$ and 2.5 mmol of $FeSO_4 \cdot 7H_2O$, and 5 mmol of $NiSO_4 \cdot 6H_2O$ without $FeSO_4 \cdot 7H_2O$, respectively. The EDS results reveal that the proportions of Ni and Fe in the NiFeP

electrocatalysts exhibit a positive correlation with the concentration of the respective salts in the electroless deposition bath.

The catalytic performance and electrochemical properties of the as-prepared catalyst for the HER were assessed electrochemically in a 1.0 M $K_2CO_3$ solution (Fig. 1). The LSV curves of the as-prepared catalyst, shown in Fig. 1a, demonstrate the excellent catalytic HER performance of the $Ni_{0.79}Fe_{0.08}P_{0.13}$ electrocatalyst, achieving overpotentials of 237 and 470 mV to supply current densities of −100 and −500 mA $cm^{-2}$, respectively. This performance is comparable to that of state-of-the-art Pt/C coatings on AEMs, which exhibit overpotentials of 259 and 427 mV to deliver current densities of −100 and −500 mA $cm^{-2}$, respectively. Notably, the catalytic performance of the $Ni_{0.79}Fe_{0.08}P_{0.13}$ electrocatalyst is superior to that of $Ni_{0.74}Fe_{0.12}P_{0.14}$, $Ni_{0.84}Fe_{0.07}P_{0.09}$, and $Ni_{0.85}P_{0.15}$ electrocatalysts. This enhanced activity of the $Ni_{0.79}Fe_{0.08}P_{0.13}$ electrocatalyst can be attributed to its optimal Fe content, which fine-tunes the electronic structure to be ideal for the HER and adjusts the crystallinity to create beneficial amorphous/crystalline interfaces, thus introducing numerous active sites.[25] The electronic structure and crystallinity of the as-prepared electrocatalysts will be discussed in more detail later in this work. To further investigate the HER kinetics of the as-prepared CCM cathode, the Tafel slopes were calculated from the LSV curves near the onset potential range (Fig. 1b). Compared with the Tafel slope of the $Ni_{0.85}P_{0.15}$ electrocatalyst (280 mV $dec^{-1}$), the Tafel slopes of the $Ni_{0.74}Fe_{0.12}P_{0.14}$, $Ni_{0.79}Fe_{0.08}P_{0.13}$, and $Ni_{0.84}Fe_{0.07}P_{0.09}$ electrocatalysts decrease to 171, 178, and 205 mV $dec^{-1}$, respectively, indicating a faster HER kinetics. Interestingly, the overall HER kinetics of the NiFeP electrocatalysts exhibit a negative correlation with the Ni/Fe ratio. The state-of-the-art Pt/C demonstrates a larger Tafel slope of 205 mV $dec^{-1}$ than that of the $Ni_{0.79}Fe_{0.08}P_{0.13}$ electrocatalyst, validating the favorable kinetics of the $Ni_{0.79}Fe_{0.08}P_{0.13}$ electrocatalyst for the HER. In addition, the faradaic efficiency (FE) of the as-prepared electrocatalysts on the AEM was calculated from the ratio of the experimentally quantified $H_2$ gas to the theoretically calculated $H_2$ gas, as shown in Fig. S3.† All as-prepared electrocatalysts on AEMs showed a high FE, and the FEs of Pt/C, $Ni_{0.74}Fe_{0.12}P_{0.14}$, $Ni_{0.79}Fe_{0.08}P_{0.13}$, and $Ni_{0.84}Fe_{0.07}P_{0.09}$, and $Ni_{0.85}P_{0.15}$ electrocatalysts are 99.8%, 98.8%, 98.9%, 97.4% and 99.5%, respectively. The EIS results of the $Ni_{0.79}Fe_{0.08}P_{0.13}$ and $Ni_{0.85}P_{0.15}$ electrocatalysts (Fig. S4 and Table S2†) were obtained using a membrane test machine to assess the resistivity of the electroless-deposited metal films. For comparison, the EIS results of the pure AEM were also measured. The $R_{ohm}$ of the $Ni_{0.85}P_{0.15}$ electrocatalyst (1.5 Ω) is smaller than that of the $Ni_{0.79}Fe_{0.08}P_{0.13}$ electrocatalyst (2.4 Ω), demonstrating the lower electrical resistivity of the $Ni_{0.79}Fe_{0.08}P_{0.13}$ electrocatalyst. This result suggests an increase in electric resistivity with the introduction of Fe, consistent with previous findings.[26] The CP measurements reveal the long-term stability of the $Ni_{0.79}Fe_{0.08}P_{0.13}$ electrocatalyst and Pt/C for the HER at a current density of −500 mA $cm^{-2}$ (Fig. 1c). The overpotential of Pt/C changes from its

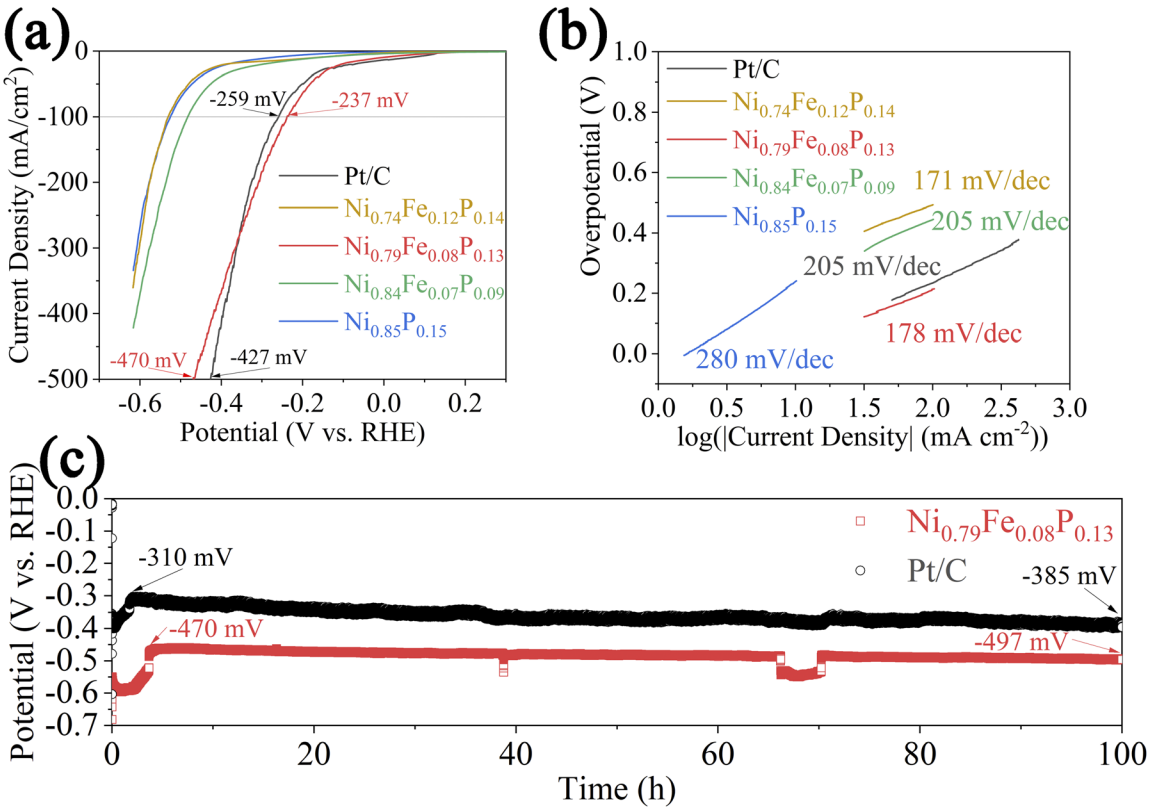


Fig. 1 Linear sweep voltammetry curves (a), Tafel slopes (b) and chronopotentiometry (c) of the as-prepared catalyst-coated membrane (CCM) cathode at a current density of −500 mA $cm^{-2}$.

 

best value of 310 mV to 385 mV over 100 h, exhibiting an overpotential increase of 24.2%. The overpotential of the $Ni_{0.79}Fe_{0.08}P_{0.13}$ electrocatalyst changes from its best value of 470 mV to 497 mV by the end, illustrating an overpotential increase of 5.7% over the same period. These results highlight the excellent stability of the $Ni_{0.79}Fe_{0.08}P_{0.13}$ electrocatalyst for the HER. During the stability test, the overpotential fluctuations at approximately 40 h and 65 h are attributed to the refreshment of the electrolyte. The improved stability of the $Ni_{0.79}Fe_{0.08}P_{0.13}$ electrocatalyst for the HER compared to Pt/C films is attributed to its ionomer/binder-free structure.[19] The LSV and CP curves of the YNU cell are shown in Fig. S5.† In Fig. S5a,† the voltages with Pt/C and $Ni_{0.79}Fe_{0.08}P_{0.13}$-integrated cells at a current density of 0.5 A $cm^{-2}$ are 2.25 V and 2.46 V, respectively. As shown in Fig. S5b,† the resulting potential in the durability test was achieved when the current density was constant at 0.5 A $cm^{-2}$. During the first 4.5 h, the cell voltage of the Pt/C|AEM|NF cell severely increased from 2.24 V to 2.4 V. The voltage of the $Ni_{0.79}Fe_{0.08}P_{0.13}$|AEM|NF cell increased from 2.27 V to 2.38 V during 100 h, revealing the good durability of the $Ni_{0.79}Fe_{0.08}P_{0.13}$ electrocatalyst towards the HER. It is noted that the cell voltages of the YNU cell can be significantly improved, as no electrocatalyst was applied on anode side in the setup.

To further investigate the electrochemical surface area (ECSA), the cyclic voltammetry experiments were conducted at scan rates ranging from 20 mV $s^{-1}$ to 100 mV $s^{-1}$ (Fig. S6a–c†), and the double-layered capacity ($C_{dl}$) was calculated (Fig. S6d†). The Pt/C fabricated *via* the spraying method exhibits the highest $C_{dl}$ of 1.65 mF $cm^{-2}$, compared to 1.31 and 1.55 mF $cm^{-2}$ for the $Ni_{0.79}Fe_{0.08}P_{0.13}$ and $Ni_{0.85}P_{0.15}$ electrocatalysts, respectively. The lower $C_{dl}$ values of the $Ni_{0.79}Fe_{0.08}P_{0.13}$ and $Ni_{0.85}P_{0.15}$ electrocatalysts can be attributed to the relatively dense nature of the electroless deposits. The electrochemical measurement results are summarized in Table S3.† To determine the origin of the excellent catalytic performance of the $Ni_{0.79}Fe_{0.08}P_{0.13}$ electrocatalyst, further characterization was conducted.

Fig. 2a and b demonstrate the surface and cross-sectional views, respectively, of the $Ni_{0.79}Fe_{0.08}P_{0.13}$ electrocatalyst. As shown in Fig. 2a, several spherical particles, each composed of small grains, are observed on the $Ni_{0.79}Fe_{0.08}P_{0.13}$ electrocatalyst surface. The boundaries of the particles serve as a channel for hydrogen diffusion during the HER.[27] The acceleration effects of grain boundaries on hydrogen diffusion through Ni-based metal membranes have been reported in previous studies.[28–31] During the HER, water molecules diffuse through the AEM from the anode to the cathode, reaching the interface between the

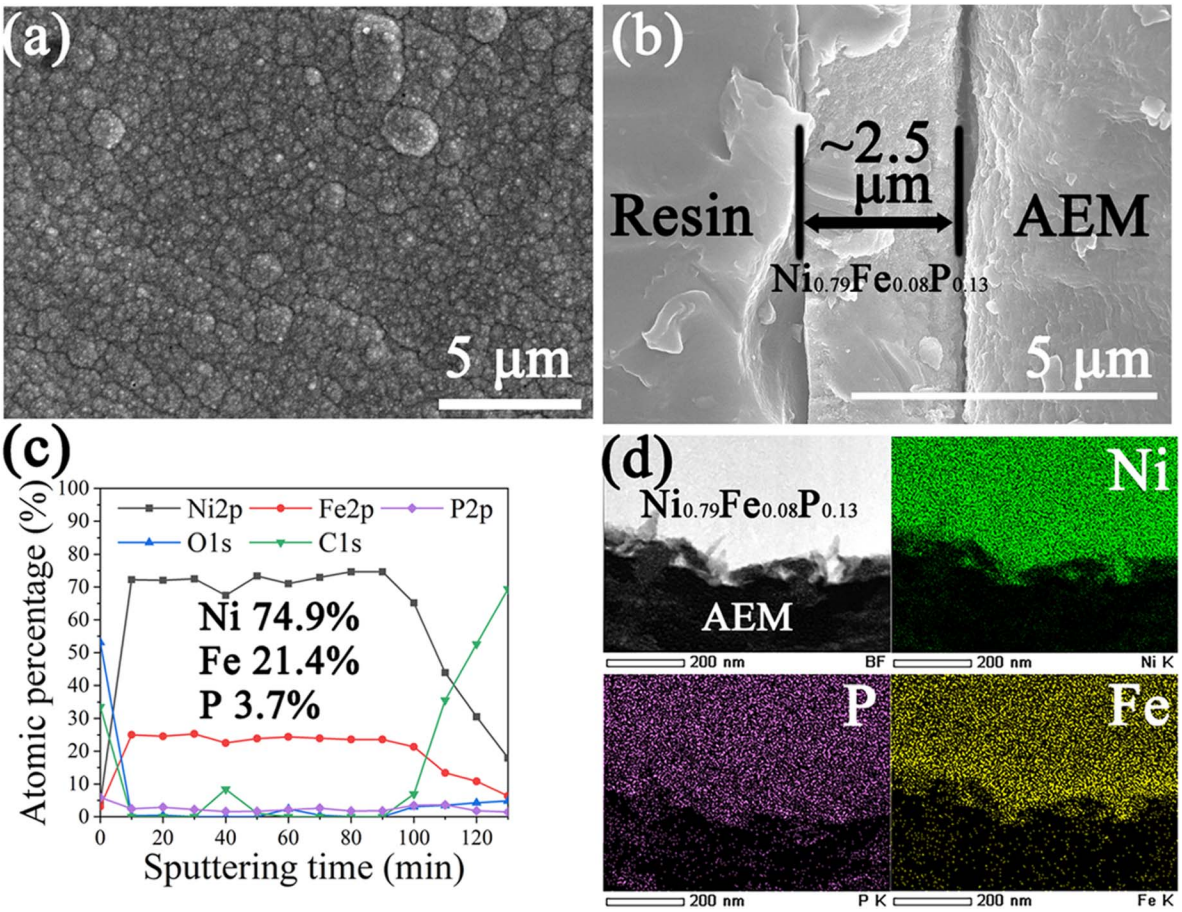


Fig. 2 Scanning electron microscopy image (a), cross-sectional image (b), calculated composition using the X-ray photoelectron spectroscopy depth profile (c) and energy dispersive X-ray spectroscopy mapping (d) of the $Ni_{0.79}Fe_{0.08}P_{0.13}$ electrocatalyst. (Here AEM refers to the anion exchange membrane).

AEM and the catalyst layer, where the HER occurs. The morphology formed during the initial stage of electroless deposition influences the number of active sites, thereby playing a crucial role in the catalytic performance of the $Ni_{0.79}Fe_{0.08}P_{0.13}$ electrocatalyst for the HER. The early stage of the electroless deposition of the $Ni_{0.79}Fe_{0.08}P_{0.13}$ electrocatalyst was investigated by varying the deposition time, followed by SEM analysis (Fig. S7†). The catalyst grains are evenly distributed on the AEM surface and grow into particles by merging with the surrounding grains. The entire surface of the exposed AEM is covered with the $Ni_{0.79}Fe_{0.08}P_{0.13}$ electrocatalyst within 30 s of electroless deposition. The SEM images of the electroless-deposited electrocatalysts are shown in Fig. S8.† Fig. S8a† illustrates the morphology of the $Ni_{0.74}Fe_{0.12}P_{0.14}$ electrocatalyst, where several spherical particles are observed. In contrast to Fig. 2a, no small grains are observed on the surface of an individual particle, resulting in a smoother particle surface. The images of the $Ni_{0.84}Fe_{0.07}P_{0.09}$ (Fig. S8b†) and $Ni_{0.85}P_{0.15}$ (Fig. S8c†) surfaces exhibit a morphology similar to that of the $Ni_{0.79}Fe_{0.08}P_{0.13}$ surface, which corresponds to a combination of spherical particles and small grains. The resin-immobilized $Ni_{0.79}Fe_{0.08}P_{0.13}$ electrocatalyst was polished to expose the cross-sectional side of the films for SEM evaluation (Fig. 2b). The thickness of the electroless-deposited $Ni_{0.79}Fe_{0.08}P_{0.13}$ electrocatalyst is approximately 2.5 μm. A magnified cross-sectional image (Fig. S9†) reveals a porous structure near the AEM, which is consistent with the SEM images of the initial deposition stage (Fig. S7†) and is expected to enhance hydrogen diffusion. To confirm the homogeneity and measure the composition of the $Ni_{0.79}Fe_{0.08}P_{0.13}$ electrocatalyst, XPS depth profiles were obtained (Fig. 2c). Ar sputtering was performed from the surface to the bottom of the $Ni_{0.79}Fe_{0.08}P_{0.13}$ electrocatalyst every 10 min. The atomic percentages of Ni, Fe, P, O, and C were calculated based on the peak areas in the high-resolution XPS spectra obtained after each sputtering step. Initially, the $Ni_{0.79}Fe_{0.08}P_{0.13}$ electrocatalyst surface exhibits significantly higher C and O percentage contents compared to Ni, Fe, and P. This is primarily attributed to the adsorption of $CO_2$ and the unavoidable surface oxidation in air. From a sputtering time of 10 min to 100 min, the calculated contents refer to the bulk area of the $Ni_{0.79}Fe_{0.08}P_{0.13}$ electrocatalyst. In the bulk region, the concentration of C and O nearly disappeared, leaving the average contents of Ni, Fe, and P measuring 74.9%, 21.4%, and 3.7%, respectively. The contents throughout the entire bulk area remain consistent, confirming the homogeneity of the $Ni_{0.79}Fe_{0.08}P_{0.13}$ electrocatalyst composition. At a sputtering time of 110 min, the C content increases, whereas the Ni, Fe, and P contents decrease, indicating the presence of an interface area between the $Ni_{0.79}Fe_{0.08}P_{0.13}$ electrocatalyst and the AEM. At this interface (sputtering time of 110 min), the calculated Ni, Fe, and P contents are 71.9%, 25%, and 3.1%, respectively, comparable to those in the bulk area. This result demonstrates the compositional homogeneity of the $Ni_{0.79}Fe_{0.08}P_{0.13}$ electrocatalyst across both the interface and bulk areas, facilitating the accurate analysis of the active sites by examining the bulk area, which exhibits characteristics similar to those of the interface area. The elemental distribution of Ni, Fe, and P in the $Ni_{0.79}Fe_{0.08}P_{0.13}$ electrocatalyst was measured by EDS mapping equipped with TEM (Fig. 2d). The uniform distribution of these elements indicates the homogeneity of the $Ni_{0.79}Fe_{0.08}P_{0.13}$ electrocatalyst near the AEM.

Crystallinity is a key factor influencing the catalytic performance of metal phosphorus toward the HER.[32,33] To investigate the crystallinity of the as-prepared NiFeP electrocatalysts, XRD and TEM analyses were conducted (Fig. 3). The XRD patterns of the pristine NiFeP electrocatalysts are shown in Fig. 3a. For the NiFeP electrocatalysts, the diffraction peaks located at $2\theta = 21.55°$ and 24.05° can be ascribed to the (110) and (200) planes of the $(CH_2)_n$ phase (JCPDS card no. 40-1995), which correspond to the AEM substrate. For $Ni_{0.79}Fe_{0.08}P_{0.13}$ and $Ni_{0.84}Fe_{0.07}P_{0.09}$ electrocatalysts, the broad peak observed near $2\theta = 44.65°$ corresponds to the (110) plane of the (Fe, Ni) phase (JCPDS card no. 37-0474), indicating that the primary phases of the $Ni_{0.79}Fe_{0.08}P_{0.13}$ and $Ni_{0.84}Fe_{0.07}P_{0.09}$ electrocatalysts correspond to the (Fe, Ni) alloys with low crystallinity. Other phases cannot be ruled out because of the high intensity of the relative peaks for $(CH_2)_n$. Furthermore, the (Fe, Ni) phases can obscure weaker peaks associated with phases with low proportions, such as the peaks for the oxidation layer and P species.[34] However, the peak for the (110) plane of the (Fe, Ni) phase is hardly observed in the $Ni_{0.74}Fe_{0.12}P_{0.14}$ electrocatalyst, revealing its amorphous nature. Comparing the peak intensity and full width at half maximum (FWHM) near $2\theta = 44.65°$ for the as-prepared NiFeP electrocatalysts, the crystallinity exhibits a negative correlation with the Fe content, consistent with previous studies.[35,36] The $Ni_{0.79}Fe_{0.08}P_{0.13}$ and $Ni_{0.84}Fe_{0.07}P_{0.09}$ electrocatalysts exhibit similar intensities and FWHM owing to their comparable Fe contents. The introduction of Fe induces the formation of an amorphous phase, creating several defects and significantly enhancing the catalytic performance of the HER.[32,37] Interestingly, the $Ni_{0.79}Fe_{0.08}P_{0.13}$ electrocatalyst exhibits significantly better catalytic performance than the $Ni_{0.84}Fe_{0.07}P_{0.09}$ electrocatalyst despite their comparable crystallinities and Fe contents. This is attributed to the synergistic effects of the introduced Fe and P, as the beneficial effects of P species on the HER activities of the electrocatalysts have been widely reported.[38–40] Partially enlarged XRD patterns of the as-prepared NiFeP electrocatalysts are shown in Fig. S10a.† A negative shift in the peaks of the (110) plane is observed for the as-prepared NiFeP electrocatalysts, with $2\theta$ angles of 44.34°, 44.4°, and 44.54° for $Ni_{0.74}Fe_{0.12}P_{0.14}$, $Ni_{0.79}Fe_{0.08}P_{0.13}$, and $Ni_{0.84}Fe_{0.07}P_{0.09}$ electrocatalysts, respectively. The negative peak shift is attributed to the substitution of Ni with Fe, which has a larger atomic radius than Ni.[35,41,42] A comparison of the XRD patterns of the $Ni_{0.79}Fe_{0.08}P_{0.13}$ electrocatalyst before and after the prolonged HER durability test is shown in Fig. S10b.† No significant changes are observed, indicating the stability of the $Ni_{0.79}Fe_{0.08}P_{0.13}$ electrocatalyst during the HER. A high-resolution TEM (HRTEM) image of the area near the interface between the AEM and $Ni_{0.79}Fe_{0.08}P_{0.13}$ electrocatalyst is shown in Fig. 3b, revealing a mixture of crystalline and amorphous features of the $Ni_{0.79}Fe_{0.08}P_{0.13}$ electrocatalyst. To further analyze the species of lattice fringes shown in the HRTEM image, the distances between the lattice fringes were measured using software. The

 

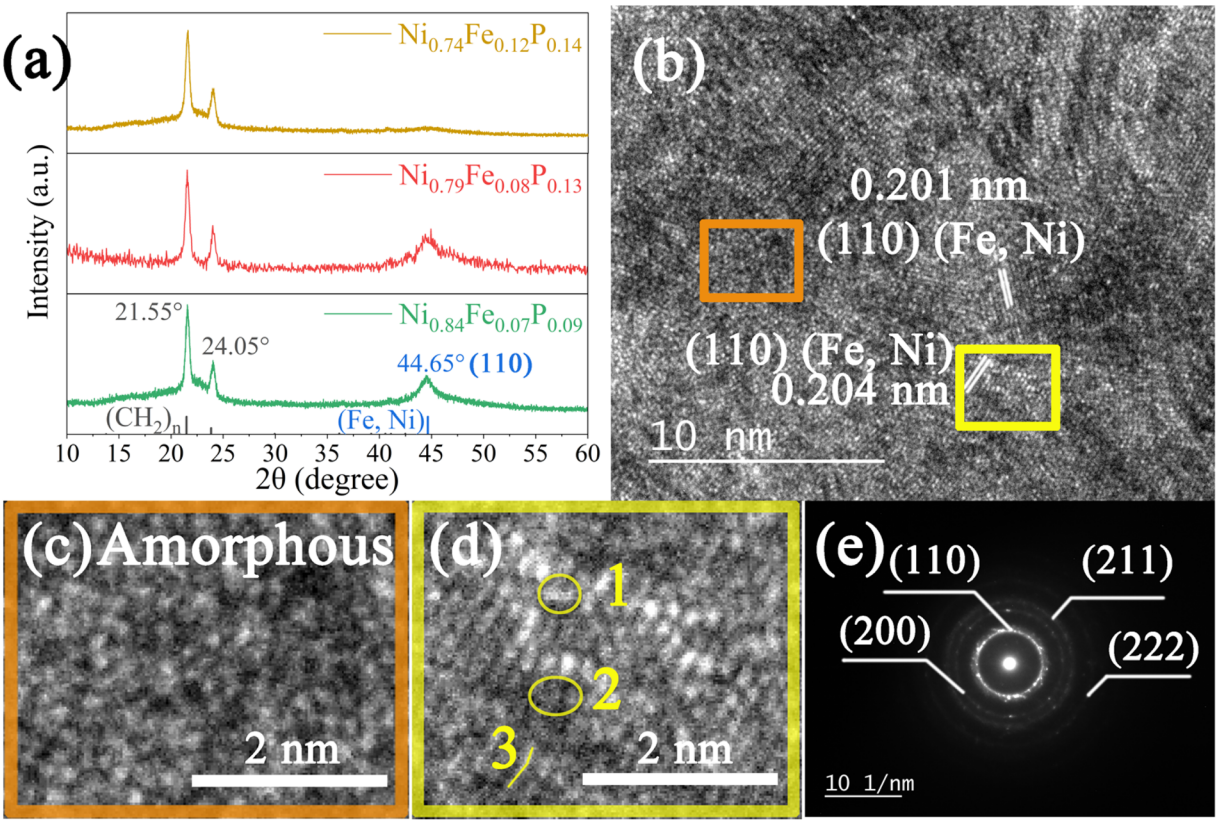


Fig. 3 X-ray diffraction patterns (a) of the as-prepared NiFeP electrocatalysts, high-resolution transmission electron microscopy (TEM) image (b), magnification of the selected area (c and d), and selected area electron diffraction pattern (e) of the TEM region of the $Ni_{0.79}Fe_{0.08}P_{0.13}$ electrocatalyst.

calculated distances of 0.201 and 0.204 nm correspond well with the lattice fringe distance of the (110) plane of the (Fe, Ni) phase, in accordance with the XRD results. The orange-labelled square magnified area (Fig. 3c) illustrates the amorphous area generated in the $Ni_{0.79}Fe_{0.08}P_{0.13}$ electrocatalyst. The amorphous structures are advantageous to the performance of Ni-based material toward the HER as they provide a larger ECSA, better diffusion ability of electrolyte, higher corrosion resistance in alkaline medium, and more defects in the structure.[32] The magnified yellow-labeled area (Fig. 3d) highlights three distinct structural features in the crystalline region: the aggregated adjacent lattice fringes (area labeled 1), the vacancies of lattice fringes (area labeled 2), and the bent lattice fringes (area labeled 3). These specific structures are beneficial for HER performance, as they provide a high number of defect sites.[43] Such defects can enhance catalytic activity toward the HER by enriching the coordinatively unsaturated atoms, modulating the electronic structures, and supporting the potential catalytically active species during the HER.[44] To further understand the TEM image, the SAED pattern of the analyzed TEM area is shown in Fig. 3e. The pattern displays an indistinct diffraction halo and relatively distinct rings, corresponding to the (110), (200), (211), and (222) planes, respectively. This indicates the coexistence of crystalline and amorphous (Fe, Ni) phases.[45] To further investigate the crystallinity, FIB-TEM was conducted to obtain a cross-sectional image of a $Ni_{0.79}Fe_{0.08}P_{0.13}$ electrocatalyst flake (Fig. S11a†). For comparison, the HR-TEM image and SAED pattern of the area far from the AEM are shown in Fig. S11b.† Interestingly, Fig. S11b† depicts a more amorphous region compared to Fig. 3b, which demonstrates decreased crystallinity from the bottom to the surface during the electroless deposition process. The inset (SAED pattern) in Fig. S11b† also shows less distinct rings, confirming the change in crystallinity with depth. These results suggest the presence of a significant number of amorphous/crystalline interfaces at the interface of the AEM and $Ni_{0.79}Fe_{0.08}P_{0.13}$ electrocatalyst, which have been demonstrated to enhance the HER performance of Ni-based materials.[46–48] Moreover, the region farther from the AEM exhibits lower crystallinity, which promotes easier and faster hydrogen diffusion owing to the disordered structure. This variation in crystallinity of the $Ni_{0.79}Fe_{0.08}P_{0.13}$ electrocatalyst with depth aligns with the ideal conditions for achieving better catalytic performance toward the HER.[28] In summary, the electroless-deposited $Ni_{0.79}Fe_{0.08}P_{0.13}$ electrocatalyst illustrates favorable crystallinity by creating a significant number of amorphous/crystalline interfaces near the AEM, which enhances its catalytic performance towards the HER. Additionally, hydrogen diffusion is facilitated by the reduced crystallinity farther from the AEM.

The survey and high-resolution XPS profiles of the bulk area (sputtering time of 70 min) of the $Ni_{0.79}Fe_{0.08}P_{0.13}$ and $Ni_{0.85}P_{0.15}$ electrocatalysts are shown in Fig. 4. The survey spectrum of the

$Ni_{0.79}Fe_{0.08}P_{0.13}$ electrocatalyst (Fig. 4a) demonstrates the Ni 2p, Fe 2p, and P 2p peaks for the $Ni_{0.79}Fe_{0.08}P_{0.13}$ electrocatalyst, validating the successful synthesis of the $Ni_{0.79}Fe_{0.08}P_{0.13}$ electrocatalyst on the AEM surface. The relatively low intensity of the P 2p spectrum is attributed to the low P content in the $Ni_{0.79}Fe_{0.08}P_{0.13}$ electrocatalyst. Understanding the detailed species and electronic structure of the $Ni_{0.79}Fe_{0.08}P_{0.13}$ electrocatalyst is crucial to enhance its catalytic performance in the HER. In the Ni 2p spectrum of the $Ni_{0.79}Fe_{0.08}P_{0.13}$ electrocatalyst (Fig. 4b), the peak observed at a binding energy (BE) of 852.65 eV can be attributed to the metallic Ni in the (Fe, Ni) alloy.[49] The peak located at a binding energy of 854.53 eV can be ascribed to the existence of Ni(II) species.[50] The satellite peak of Ni $2p_{3/2}$ is observed at a binding energy of 859.28 eV. The Ni 2p spectrum of the $Ni_{0.85}P_{0.15}$ electrocatalyst was compared with that of the $Ni_{0.79}Fe_{0.08}P_{0.13}$ electrocatalyst, showing the peaks of metallic Ni and Ni(II) species, and satellite peaks at binding energies of 853.02, 854.9 eV, and 859.77 eV, respectively. The Ni 2p spectrum of the $Ni_{0.79}Fe_{0.08}P_{0.13}$ electrocatalyst shows a negative shift of 0.37 eV compared to the $Ni_{0.85}P_{0.15}$ electrocatalyst, indicating that the Ni sites receive electrons upon the introduction of Fe. In Fig. 4c, the Fe 2p spectrum for the $Ni_{0.79}Fe_{0.08}P_{0.13}$ electrocatalyst illustrates the existence of metallic Fe and Fe(III), and satellite peaks at the binding energies of 707.28 eV, 712.28 eV, and 720.4 eV, respectively.[49,51,52] The standard binding energy for metallic Fe is 707.0 eV, which confirms the positive shift of binding energy by 0.28 eV in the Fe 2p spectrum of the $Ni_{0.79}Fe_{0.08}P_{0.13}$ electrocatalyst. This indicates the loss of electrons from the Fe sites in the $Ni_{0.79}Fe_{0.08}P_{0.13}$ electrocatalyst. The high-resolution XPS spectra of P 2p for the $Ni_{0.79}Fe_{0.08}P_{0.13}$ and $Ni_{0.85}P_{0.15}$ electrocatalysts are presented in Fig. 4d. For the $Ni_{0.79}Fe_{0.08}P_{0.13}$ electrocatalyst, a prominent peak at a binding energy of 129.9 eV and a smaller peak at a binding energy of 133.4 eV are observed, which can be attributed to the metal–phosphide bond and phosphate, respectively.[50] The intensity of the phosphate peak is significantly weaker compared to that of the phosphide, which is attributed to the low content of phosphate species in the $Ni_{0.79}Fe_{0.08}P_{0.13}$ electrocatalyst. Comparing the binding energies of the phosphide peaks for the $Ni_{0.79}Fe_{0.08}P_{0.13}$ electrocatalyst (129.9 eV) and $Ni_{0.85}P_{0.15}$ electrocatalyst (130.02 eV) reveals that the P sites receive electrons upon Fe introduction. The modulation of the electronic structure is caused by the combined effects of the electronegativity differences between elements and defect structures, which can effectively induce alterations in the localized crystal structure, composition, and

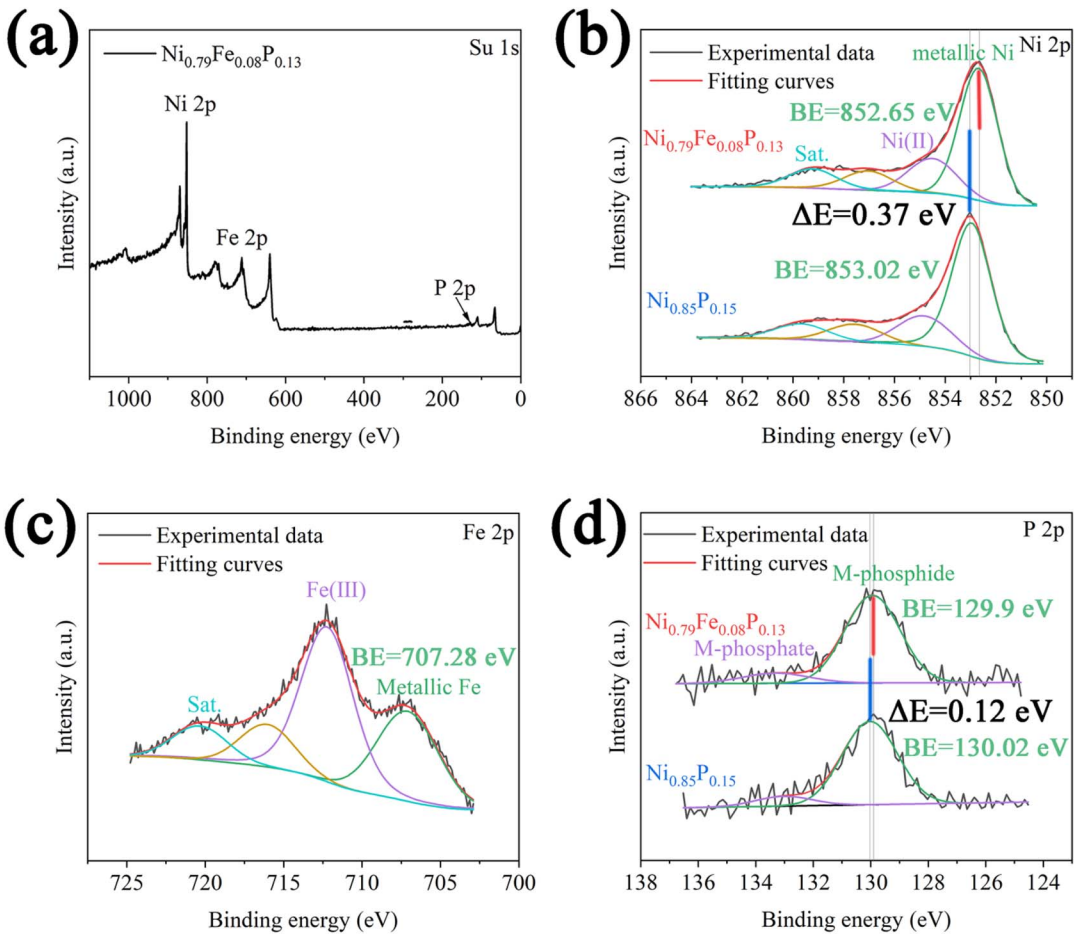


Fig. 4 Survey spectrum of the $Ni_{0.79}Fe_{0.08}P_{0.13}$ electrocatalyst (a) and high-resolution X-ray photoelectron spectra of Ni 2p (b), Fe 2p (c) and P 2p (d) of the $Ni_{0.79}Fe_{0.08}P_{0.13}$ and $Ni_{0.85}P_{0.15}$ electrocatalysts.

 

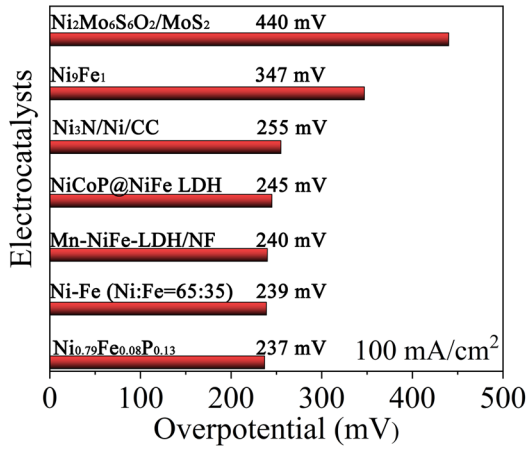


Fig. 5 Comparison of the overpotentials required to drive a current density of −100 mA $cm^{-2}$ for $Ni_{0.79}Fe_{0.08}P_{0.13}$ and other reported HER electrocatalysts.

chemical states.[44,53,54] As a result, the introduction of Fe alters the electronic structure of the $Ni_{0.79}Fe_{0.08}P_{0.13}$ electrocatalyst, with electrons generally being transferred from the Fe sites to the Ni and P sites. In Ni–P-based materials, the Ni sites are usually positively charged, the P sites are negatively charged, and the Ni and P sites act as hydride and proton acceptors to enhance HER performance.[38,53] For the $Ni_{0.79}Fe_{0.08}P_{0.13}$ electrocatalyst, the introduction of Fe slightly increases the negative charge on the P sites, which enhances their ability to trap protons and facilitates their further reaction during the HER. Interestingly, the Ni sites are slightly negatively charged, and the introduced Fe sites are positively charged. The altered electronic structure suggests that the Fe sites in the $Ni_{0.79}Fe_{0.08}P_{0.13}$ electrocatalyst play an essential role as hydride acceptors during the HER, which facilitates the adsorption and dissociation of water molecules. Additionally, Ni sites can partially function as proton acceptors, contributing to the increased HER activity.[55–57]

Finally, the catalytic performance of the $Ni_{0.79}Fe_{0.08}P_{0.13}$ electrocatalyst towards the HER at a current density of −100 mA $cm^{-2}$ is compared with that of other Ni-based electrocatalysts reported in recent years, as shown in Fig. 5.[58–63] Catalytic performances of other electrocatalysts are reported in 1.0 M KOH or NaOH solutions. The $Ni_{0.79}Fe_{0.08}P_{0.13}$ electrocatalyst exhibits superior catalytic performance compared with other electrocatalysts in solutions with lower alkalinity, demonstrating its potential as a promising candidate for HER electrocatalysis.

## Conclusions

The NiFeP electrocatalysts were successfully synthesized on an AEM surface as CCM cathodes *via* a facile Pd-catalyzed electroless deposition process. The $Ni_{0.79}Fe_{0.08}P_{0.13}$ electrocatalyst exhibited enhanced catalytic performance for the HER in 1.0 M $K_2CO_3$ solution, achieving an overpotential of 470 mV at a current density of −500 mA $cm^{-2}$. The enhanced catalytic performance is attributed to two main factors. First, the introduction of Fe altered the electronic structure of the $Ni_{0.79}Fe_{0.08}P_{0.13}$ electrocatalyst, which effectively enhanced its intrinsic activity by absorbing water molecules and protons and transforming them into other intermediates. Second, the $Ni_{0.79}Fe_{0.08}P_{0.13}$ electrocatalyst exhibited an optimal crystallinity distribution after introducing Fe. The increased number of amorphous/crystalline interfaces between the AEM and $Ni_{0.79}Fe_{0.08}P_{0.13}$ electrocatalyst significantly improved the HER activity. Lower crystallinity was observed farther from the interface, which could effectively facilitate hydrogen diffusion. The $Ni_{0.79}Fe_{0.08}P_{0.13}$ electrocatalyst exhibited excellent stability toward the HER with only a 5.7% increase in overpotential after 100 h, which was attributed to the ionomer-/binder-free structure of the as-prepared $Ni_{0.79}Fe_{0.08}P_{0.13}$ electrocatalyst. This work advances the design and synthesis of non-noble metal-based ionomer-/binder-free CCM cathodes for AEM water splitting devices. It contributes to the development of large-scale AEM water electrolysis systems.

## Data availability

The data supporting this article have been included as part of the ESI.†

## Author contributions

Kaiming Guo: investigation, methodology, conceptualization, formal analysis, and writing of the original draft. Masahiro Kunimoto: conceptualization, investigation, methodology, writing, reviewing, and editing. Takayuki Homma: conceptualization, writing, reviewing and editing, supervision, project administration.

## Conflicts of interest

There are no conflicts to declare.

## References

1 M. Ashraf, N. Ullah, I. Khan, W. Tremel, S. Ahmad and M. N. Tahir, *Chem. Rev.*, 2023, **123**, 4443–4509.
2 H. Wang, X. Cheng and Y. Tong, *J. Colloid Interface Sci.*, 2023, **629**, 155–164.
3 J. He, Y. Tong, Z. Wang, G. Zhou, X. Ren, J. Zhu, N. Zhang, L. Chen and P. Chen, *Proc. Natl. Acad. Sci. U. S. A.*, 2024, **121**, e2405846121.
4 C. Liu, Z. Geng, X. Wang, W. Liu, Y. Wang, Q. Xia, W. Li, L. Jin and C. Zhang, *J. Energy Chem.*, 2024, **90**, 348–369.
5 H. A. Miller, K. Bouzek, J. Hnat, S. Loos, C. I. Bernäcker, T. Weißgärber, L. Röntzsch and J. Meier-Haack, *Sustain. Energy Fuels*, 2020, **4**, 2114–2133.
6 M. Riemer, S. Duval-Dachary and T. M. Bachmann, *Sustain. Energy Technol. Assessments*, 2023, **56**, 103086.
7 B. Motealleh, Z. Liu, R. I. Masel, J. P. Sculley, Z. R. Ni and L. Meroueh, *Int. J. Hydrogen Energy*, 2021, **46**, 3379–3386.

8 Y. Zheng, W. Ma, A. Serban, A. Allushi and X. Hu, *Angew. Chem., Int. Ed.*, 2024, e202413698.
9 Y. Luo, Z. Zhang, M. Chhowalla and B. Liu, *Adv. Mater.*, 2022, **34**, 2108133.
10 Y. Chen, Q. Li, Y. Lin, J. Liu, J. Pan, J. Hu and X. Xu, *Nat. Commun.*, 2024, **15**, 7278.
11 Z. Wei, M. Guo and Q. Zhang, *Appl. Catal., B*, 2023, **322**, 122101.
12 W. Zhang, Y. Zou, H. Liu, S. Chen, X. Wang, H. Zhang, X. She and D. Yang, *Nano Energy*, 2019, **56**, 813–822.
13 H. Ito, N. Miyazaki, S. Sugiyama, M. Ishida, Y. Nakamura, S. Iwasaki, Y. Hasegawa and A. Nakano, *J. Appl. Electrochem.*, 2018, **48**, 305–316.
14 M. Faraj, E. Elia, M. Boccia, A. Filpi, A. Pucci and F. Ciardelli, *J. Polym. Sci., Part A: Polym. Chem.*, 2011, **49**, 3437–3447.
15 J. E. Park, S. Y. Kang, S.-H. Oh, J. K. Kim, M. S. Lim, C.-Y. Ahn, Y.-H. Cho and Y.-E. Sung, *Electrochim. Acta*, 2019, **295**, 99–106.
16 S. Koch, P. A. Heizmann, S. K. Kilian, B. Britton, S. Holdcroft, M. Breitwieser and S. Vierrath, *J. Mater. Chem. A*, 2021, **9**, 15744–15754.
17 Y. Leng, G. Chen, A. J. Mendoza, T. B. Tighe, M. A. Hickner and C.-Y. Wang, *J. Am. Chem. Soc.*, 2012, **134**, 9054–9057.
18 T. Fujimura, M. Kunimoto, Y. Fukunaka, H. Ito and T. Homma, *Electrochemistry*, 2021, **89**, 192–196.
19 T.-H. Kong, P. Thangavel, S. Shin, S. Kwon, H. Choi, H. Lee, N. Park, J.-J. Woo and Y. Kwon, *ACS Energy Lett.*, 2023, **8**, 4666–4673.
20 C. C. Pavel, F. Cecconi, C. Emiliani, S. Santiccioli, A. Scaffidi, S. Catanorchi and M. Comotti, *Angew. Chem., Int. Ed.*, 2014, **53**, 1378–1381.
21 M. Faraj, M. Boccia, H. Miller, F. Martini, S. Borsacchi, M. Geppi and A. Pucci, *Int. J. Hydrogen Energy*, 2012, **37**, 14992–15002.
22 H. Ito, N. Kawaguchi, S. Someya, T. Munakata, N. Miyazaki, M. Ishida and A. Nakano, *Int. J. Hydrogen Energy*, 2018, **43**, 17030–17039.
23 H. Ito, N. Kawaguchi, S. Someya and T. Munakata, *Electrochim. Acta*, 2019, **297**, 188–196.
24 K. Nagasawa, T. Ishida, H. Kashiwagi, Y. Sano and S. Mitsushima, *Int. J. Hydrogen Energy*, 2021, **46**, 36619–36628.
25 Y. Li, M. Li, C. Xie, Z. Ling, Y. Lv and K. Chen, *J. Alloys Compd.*, 2024, **1002**, 175328.
26 N. V. Myung and K. Nobe, *J. Electrochem. Soc.*, 2001, **148**, C136.
27 H. Iwaoka, M. Arita and Z. Horita, *Acta Mater.*, 2016, **107**, 168–177.
28 A. Oudriss, J. Creus, J. Bouhattate, E. Conforto, C. Berziou, C. Savall and X. Feaugas, *Acta Mater.*, 2012, **60**, 6814–6828.
29 A. M. Brass and A. Chanfreau, *Acta Mater.*, 1996, **44**, 3823–3831.
30 S. K. Lawrence, Y. Yagodzinskyy, H. Hänninen, E. Korhonen, F. Tuomisto, Z. D. Harris and B. P. Somerday, *Acta Mater.*, 2017, **128**, 218–226.
31 G. S. Mogilny, V. N. Shyvaniuk, S. M. Teus, L. M. Ivaskevich and V. G. Gavriljuk, *Acta Mater.*, 2020, **194**, 516–521.
32 S. Anantharaj and S. Noda, *Small*, 2020, **16**, 1905779.
33 X. Zhao, X. Chen, Y. Wang, P. Song and Y. Zhang, *Sustain. Energy Fuels*, 2020, **4**, 4733–4742.
34 K. Guo, F. Shaik, J. Yang, X. Ren and B. Jiang, *J. Electrochem. Soc.*, 2021, **168**, 062512.
35 C. Cui, Y. Liu, S. Mehdi, H. Wen, B. Zhou, J. Li and B. Li, *Appl. Catal., B*, 2020, **265**, 118612.
36 O. Dragos, H. Chiriac, N. Lupu, M. Grigoras and I. Tabakovic, *J. Electrochem. Soc.*, 2016, **163**, D83–D94.
37 G. Shao, Q. Wang, F. Miao, J. Li, Y. Li and B. Shen, *Electrochim. Acta*, 2021, **390**, 138815.
38 P. Liu and J. A. Rodriguez, *J. Am. Chem. Soc.*, 2005, **127**, 14871–14878.
39 D. Liu, G. Xu, H. Yang, H. Wang and B. Y. Xia, *Adv. Funct. Mater.*, 2023, **33**, 2208358.
40 Y. Pan, Y. Liu, J. Zhao, K. Yang, J. Liang, D. Liu, W. Hu, D. Liu, Y. Liu and C. Liu, *J. Mater. Chem. A*, 2015, **3**, 1656–1665.
41 M. Miao, R. Hou, R. Qi, Y. Yan, L. Q. Gong, K. Qi, H. Liu and B. Y. Xia, *J. Mater. Chem. A*, 2019, **7**, 18925–18931.
42 J. Zhao, N. Liao and J. Luo, *J. Mater. Chem. A*, 2023, **11**, 9682–9690.
43 S. He, C. Li, H. Chen, D. Su, B. Zhang, X. Cao, B. Wang, M. Wei, D. G. Evans and X. Duan, *Chem. Mater.*, 2013, **25**, 1040–1046.
44 J. Xie, X. Yang and Y. Xie, *Nanoscale*, 2020, **12**, 4283–4294.
45 L. Cai, B. Yan, Q. Xue, J. Li, P. Liu, X. Qi and G. Yang, *J. Mater. Chem. A*, 2022, **10**, 18939–18949.
46 X. Xu, T. Guo, J. Xia, B. Zhao, G. Su, H. Wang, M. Huang and A. Toghan, *Chem. Eng. J.*, 2021, **425**, 130514.
47 B. Zhong, S. Wan, P. Kuang, B. Cheng, L. Yu and J. Yu, *Appl. Catal., B*, 2024, **340**, 123195.
48 S. Yang, T. Wen and Y. Gong, *Int. J. Hydrogen Energy*, 2024, **68**, 834–842.
49 F. Li, Y. Li, Q. Zhuo, D. Zhou, Y. Zhao, Z. Zhao, X. Wu, Y. Shan and L. Sun, *ACS Appl. Mater. Interfaces*, 2020, **12**, 11479–11488.
50 A. Kafle, M. Kumar, D. Gupta and T. C. Nagaiah, *J. Mater. Chem. A*, 2021, **9**, 24299–24307.
51 Z. Zhang, Y. Bai, Y. He, H. Li, T. He, R. Song, Y. He, J. Song and B. Liu, *Surf. Coat. Technol.*, 2022, **448**, 128934.
52 B. Li, T. Mei, S. Du and W. Zhang, *Mater. Chem. Phys.*, 2020, **243**, 122595.
53 Y. Shi, M. Li, Y. Yu and B. Zhang, *Energy Environ. Sci.*, 2020, **13**, 4564–4582.
54 C. Xie, D. Yan, W. Chen, Y. Zou, R. Chen, S. Zang, Y. Wang, X. Yao and S. Wang, *Mater. Today*, 2019, **31**, 47–68.
55 Q. Fu, X. Wang, J. Han, J. Zhong, T. Zhang, T. Yao, C. Xu, T. Gao, S. Xi, C. Liang, L. Xu, P. Xu and B. Song, *Angew. Chem.*, 2021, **133**, 263–271.
56 V. Vij, S. Sultan, A. M. Harzandi, A. Meena, J. N. Tiwari, W.-G. Lee, T. Yoon and K. S. Kim, *ACS Catal.*, 2017, **7**, 7196–7225.
57 X. Chen, J. Wan, J. Wang, Q. Zhang, L. Gu, L. Zheng, N. Wang and R. Yu, *Adv. Mater.*, 2021, **33**, 2104764.

 

58 Z. Zhang, Y. Wu and D. Zhang, *Int. J. Hydrogen Energy*, 2022, **47**, 1425–1434.
59 Y. Ma, L. Li, Y. Zhang, N. Jian, H. Pan, J. Deng and J. Li, *J. Colloid Interface Sci.*, 2024, **663**, 971–980.
60 H. Zhang, X. Du, X. Zhang and Y. Wang, *J. Alloys Compd.*, 2023, **937**, 168412.
61 L. Xiong, Y. Qiu, H. Dong, B. Gao, X. Zhang, P. K. Chu and X. Peng, *Int. J. Hydrogen Energy*, 2024, **59**, 400–407.
62 Z. Chen, X. Liu, T. Shen, C. Wu, L. Zu and L. Zhang, *Int. J. Hydrogen Energy*, 2021, **46**, 37736–37745.
63 H. Cheng, Y. Diao, Q. Liu, L. Wei, X. Li, J. Chen and F. Wang, *Chem. Eng. J.*, 2022, **428**, 131084.